ACS Energy LETTERS

http://pubs.acs.org/journal/aelccp

Letter

Harnessing Hot Electrons in Core/Shell Quantum Dots for Photoelectrochemical Solar Energy Conversion

Published as part of ACS Energy Letters special issue "The Evolving Landscape of Energy Research: Insights from Leading Researchers".

Yisen Yao,[⊥] Guohua Mi,[⊥] Xin Tong,* Alexander O. Govorov,* Guoqi Xiang, Xin Li, Fan Cui, Ziyao Xiong, Wuyang Ren, Mengyan Dai,* and Zhiming M. Wang*

Cite This: *ACS Energy Lett.* 2026, 11, 4465−4474

Read Online

ACCESS | Metrics & More | Article Recommendations | Supporting Information

ABSTRACT: Colloidal InP/ZnSe(S) core/shell quantum dots (QDs) have exhibited exceptional optoelectronic performance in light-emitting applications, while their potential in solar energy conversion technologies is constrained by low carrier extraction efficiency. Although engineering the band structure or introducing localized states within the QD bandgap is effective to optimize charge extraction, the regulation of hot-electron dynamics within the bands has been largely neglected. In this work, we modulate the hot-electron dynamics in InP/ZnSeS QDs by incorporating Mn doping during the growth of the ZnSeS shell. Theoretical and experimental investigations both demonstrate that the introduction of Mn dopant enables efficient and directional transfer of hot electrons from InP core to ZnSeS shell before charge recombination, thus significantly improving the carrier extraction efficiency. As a result, the InP/ZnSeS:Mn QDs are utilized to fabricate solar-driven photoelectrochemical (PEC) devices, which deliver a maximum photocurrent density of 14.6 mA cm^{-2} under standard 1 sun illumination, representing a state-of-the-art performance among various QDs-based PEC systems.

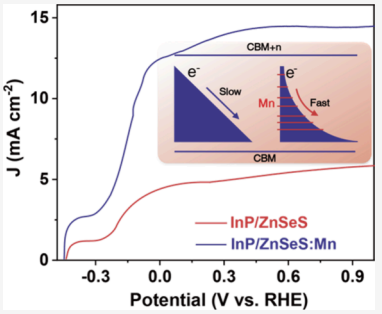

Colloidal quantum dots (QDs) are considered as promising building blocks in emerging optoelectronic technologies owing to their unique quantum confinement effect that results in size-dependent photonic characteristics.[1,2] Among these materials, III−V InP QDs have recently garnered sustained attention in light-emitting applications due to their eco-friendliness, size-tunable optical band gap, high absorption coefficients, etc.[3−8] However, bare InP QDs generally suffer from abundant surface defect/trap states caused by unsaturated bonds and intrinsic stoichiometric imbalance for suppressed emission efficiency; such deficiencies are commonly mitigated through inorganic shell (e.g., ZnSe or ZnS[9]) coating, which markedly improves their photoluminescence quantum yield (PLQY) and optical/chemical stability for device integration.[10−12] For example, Jang and co-workers achieved an external quantum efficiency (EQE) of 21.4% in InP QD-based light-emitting diodes (LEDs) through hydrofluoric acid etching of oxidized InP cores followed by successive ZnSe and ZnS shell growth, representing a major milestone for environmentally friendly QD-based display technologies.[8] More recently, by encapsulating InP cores with a thickened ZnSe interlayer and ZnS shell, Shen et al. further improved the EQE of green-emitting InP-based QD LEDs to 26.68%.[13] Despite these advances, investigations of InP/ZnSe(S) core/shell QDs have predominantly focused on improving the luminescence efficiency of QD-LEDs, whereas their potential in solar energy conversion applications, particularly in solar-driven photoelectrochemical (PEC) devices, remains fundamentally limited by the intrinsic type-I band alignment,[7,14] which impedes efficient electron transport to the outer shell region and thereby constrains subsequent carrier extraction for efficient solar-to-hydrogen energy conversion.[14−16]

In recent years, InP/ZnSe(S)-based core/shell QDs have been demonstrated as promising candidates to realize high-efficiency solar energy conversion applications.[17−20] For instance, Greta R. Patzke et al. verified the photocurrent generation in a PEC system based on InP/ZnS core/shell QDs, which yielded a photocurrent density of 0.06 mA cm^{-2} under simulated sunlight illumination.[17] Later, our group introduced Cu doping into the ZnSe shell of InP/ZnSe core/shell QDs,[6] wherein the Cu dopant-induced states led to the hole trapping for efficient photogenerated electron−hole separation/transfer, thereby increasing the maximum photocurrent density of corresponding QDs-based PEC cell to 7.4

Received: February 27, 2026
Revised: April 4, 2026
Accepted: May 11, 2026
Published: May 20, 2026

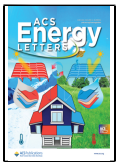

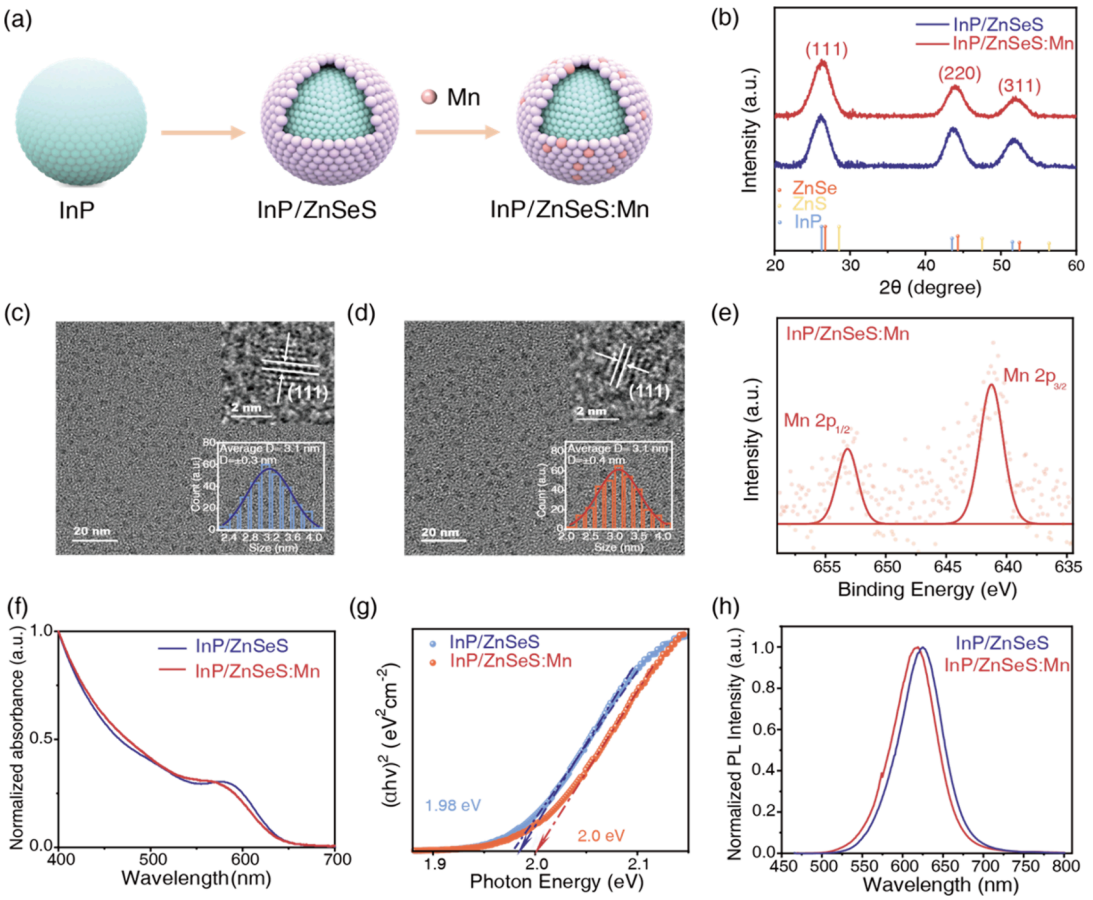

Figure 1. (**a**) Schematic diagram of the synthetic processes for the InP/ZnSeS:Mn QDs. (**b**) XRD patterns of the InP/ZnSeS and InP/ZnSeS:Mn QDs. TEM images of (**c**) InP/ZnSeS and (**d**) InP/ZnSeS:Mn QDs with corresponding inset size distributions and HRTEM images. (**e**) HRXPS spectra of Mn 2p core levels for InP/ZnSeS:Mn QDs. (**f**) Normalized absorbance, (**g**) Tauc plots, and (**h**) PL spectra of InP/ZnSeS and InP/ZnSeS:Mn QDs.

mA cm^{-2} (1 sun illumination). In another work, Rosei's group further revealed that the ZnSe shell thickness in InP/ZnSe core/shell QDs played a decisive role in photogenerated carrier transport dynamics,[18] and a maximum photocurrent density of 6.2 mA cm^{-2} was obtained in the InP/ZnSe QDs-based PEC devices with an optimal ZnSe shell thickness. Moreover, Tian's group constructed a built-in electric field via gradient In doping in the ZnSe shell to accelerate the carrier separation in InP/ZnSe core/shell QDs, thus realizing a high photocurrent density of 8.7 mA cm^{-2} in the relevant QDs-PEC cells.[19]

Although these strategies are effective in tailoring InP-based core/shell QDs for PEC applications, they predominantly rely on engineering the band structure or introducing localized states within the bandgap,[21,22] thus providing only limited control over hot electron dynamics within the conduction bands.[23] Therefore, modulation of hot-electron transport to circumvent the limitation imposed by the type-I band alignment and to promote efficient carrier extraction constitutes an essential strategy for the development of high-performing QDs-based PEC systems.[24] Since hot electrons are nonequilibrium carriers generated when photoexcited electrons occupy higher-energy states before fully relaxing to the conduction-band minimum,[16] harnessing these hot carriers is inclined to enhance the solar energy conversion efficiency of QDs.[25] Previous studies have demonstrated the hot electron generation and transport processes in various QD systems including PbSe/CdSe, Cu−In−Zn-S, and InP QDs.[16,26,27] Notably, Mn-doped QDs have emerged as a particularly promising platform for hot electron modulation. For example, Son et al. reported the extraction of hot electrons from the ZnS shell in Mn-doped CdSSe/ZnS QDs, demonstrating that tuning hot electron transport through Mn doping can boost the solar-driven photocatalytic reaction rates.[28] It is found that the Mn-doped CdSSe/ZnS QDs are a promising source of hot electrons as their quantum yield of hot electron generation could reach 35−40% under continuous white light (455 nm, excitation intensity of ~ 0.1 W/cm^2).[29] Also, the spin-exchange process in Mn-doped CdS/ZnS QDs enables efficient hot electron generation that can be utilized in a wide range of organic reactions.[30] Furthermore, the study of Mn-doped InP/ZnS core/shell QDs reveals the spin-exchange Auger recombination and hot electron relaxation mechanisms.[31] These findings collectively indicate that leveraging hot electrons, particularly through Mn doping strategies, can effectively overcome the confinement of photogenerated carriers in InP/ZnSe(S) core/shell QDs, thereby enabling efficient carrier extraction and photocurrent generation in QDs-based PEC devices.

In this work, we demonstrate a facile strategy to harness the hot electrons in InP/ZnSeS QDs by incorporating the Mn dopant during ZnSeS shell layer growth. It is revealed that such Mn doping enables efficient extraction of photogenerated hot electrons from the InP core toward the ZnSeS shell region. Theoretical calculations demonstrate the Mn doping-induced

https://doi.org/10.1021/acsenergylett.6c00616
ACS Energy Lett. 2026, 11, 4465−4474

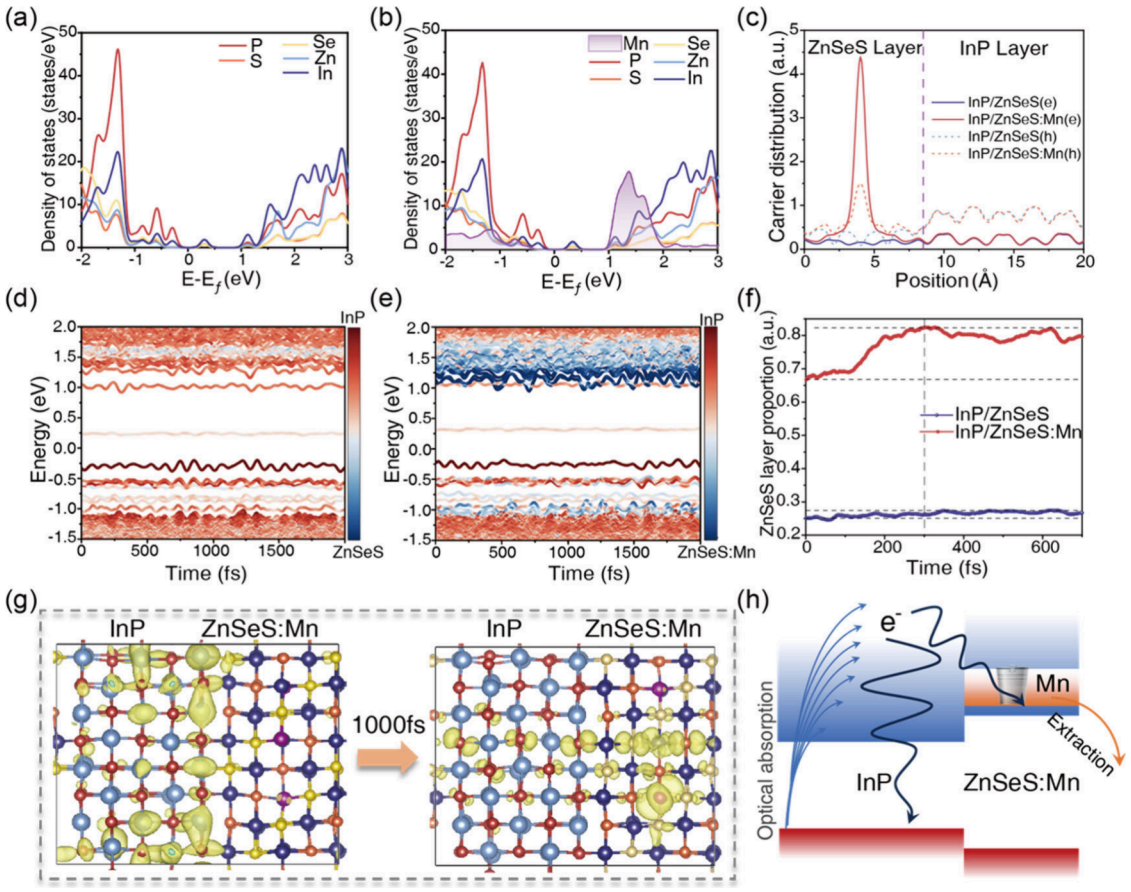

Figure 2. Calculated DOS of (**a**) InP/ZnSeS and (**b**) InP/ZnSeS:Mn heterostructures. (**c**) The spatial distribution of electrons and holes in InP/ZnSeS and InP/ZnSeS:Mn heterostructures. (**d**, **e**) Simulated time evolutions of the energy states near the Fermi level in (**d**) InP/ZnSeS and (**e**) InP/ZnSeS:Mn heterostructures. (**f**) Time-dependent spatial localization of electrons from CBM + 0.3 eV to CBM for InP/ZnSeS and InP/ZnSeS:Mn heterostructures (0.3 eV was chosen because it spans the region of the conduction band associated with the largest internal energy separation, while maintaining a reasonable computational cost). (**g**) Time-dependent spatial localization of electrons from CBM + 0.6 eV to CBM in InP/ZnSeS:Mn heterostructure, as marked in the crystal structure. Here, we present the electron distribution at 0 and 1000 fs. (**h**) Schematic diagram of photogenerated carrier transport mechanism in QDs. The intraband Mn doping states are found to function as collection sites for photogenerated carriers.

hot electron transport pathways enabling ultrafast crossing of the InP/ZnSeS:Mn QDs' interface and outward transport prior to electron−hole recombination. Transient absorption spectroscopy (TAS) further confirms a pronounced acceleration of hot electron dynamics upon Mn incorporation in the InP/ZnSeS QDs. Leveraging this hot electron modulation mechanism, the fabricated InP/ZnSeS:Mn QDs-based PEC devices delivered a maximum photocurrent density of 14.6 mA cm^{-2} under standard 1 sun illumination (AM 1.5G, 100 mW cm^{-2}), representing a state-of-the-art level of performance among environment-friendly QDs-based PEC systems. This work offers a viable strategy to harness hot electrons and mitigate the intrinsic carrier extraction limitation imposed by type-I band alignment in InP-based core/shell QDs, establishing a general design paradigm to achieve future low-cost, eco-friendly, and high-efficiency QDs-based solar energy conversion systems.

Figure 1a presents the schematic illustration of synthetic procedures for InP/ZnSeS:Mn QDs, in which the Mn doping in InP/ZnSeS QDs was achieved via a one-pot synthesis method involving the incorporation of Mn precursors in the ZnSeS layer.[4] The X-ray diffraction (XRD) patterns of as-prepared QDs are shown in Figure 1b, where the undoped InP/ZnSeS QDs exhibit three distinct diffraction peaks located between the (111), (220), and (311) planes of InP and alloyed ZnSeS, indicating the successful growth of a ZnSeS layer on InP QDs.[6] Considering the slight XRD peak shift and the low contents of Zn, Se, and S elements in inductively coupled plasma atomic emission spectroscopy (ICP-OES) results (Table S1), the coating of a relatively thin ZnSeS layer on InP QDs is verified.[20,21] After Mn doping, the XRD peak positions of InP/ZnSeS:Mn QDs show no obvious shift relative to the undoped sample, indicating that Mn incorporation does not alter the overall crystal structure of InP/ZnSeS QDs. As exhibited in Figure 1c, the transmission electron microscopy (TEM) images of undoped InP/ZnSeS QDs show approximately spherical particles with an average diameter of ∼ 3.1 ± 0.3 nm. Additionally, the inset high-resolution TEM (HRTEM) image exhibits the measured lattice fringes between the (111) plane of InP and alloyed ZnSeS, which is consistent with the XRD analysis.[4] In parallel, the Mn-doped InP/ZnSeS QDs retain spherical morphology with a similar size distribution (Figure 1d) and the lattice parameters observed in the HRTEM image remain nearly the same as those of the undoped QD sample, indicating that Mn incorporation occurs without causing significant lattice distortion,[32,33] which is in accordance with the XRD results of QDs. Besides, the X-ray photoelectron spectroscopy (XPS)

https://doi.org/10.1021/acsenergylett.6c00616
ACS Energy Lett. 2026, 11, 4465−4474

analysis further verifies the presence of In, P, Zn, Se, and S in both types of QDs (Figure S1),[19] wherein the Mn 2p core level peaks in the high-resolution XPS (HRXPS) spectra of the doped QD sample provide direct evidence of the successful Mn incorporation in InP/ZnSeS QDs (Figure 1e).[34]

Figure 1f-h shows the UV−vis absorbance spectra, Tauc plots, and PL spectra of InP/ZnSeS and InP/ZnSeS:Mn QDs, respectively. It is revealed that doping Mn into the InP/ZnSeS QDs has a minimal effect on their light absorbance (Figure 1f). Consistently, the Tauc plots (Figure 1g) of InP/ZnSeS and InP/ZnSeS:Mn QDs show similar estimated optical bandgaps of ∼ 1.98 eV and ∼ 2.0 eV, respectively (Figure 1h). Additionally, the PL emission peaks were observed at 625 nm for InP/ZnSeS and 621 nm for InP/ZnSeS:Mn QDs; such blue-shift phenomenon is in agreement with the shifting trend of their absorption spectra (Figure 1f).

In general, the Mn-introduced intraband states are difficult to resolve using conventional experimental techniques and have therefore been largely overlooked, thus limiting the physical understanding of photogenerated carriers dynamics in Mn-doped QDs.[35,36] In this case, we further elucidate the regulatory role of Mn-induced intraband doping states on carrier transport (e.g., hot electrons) of InP/ZnSeS QDs by combining the first-principles calculations, Ab initio molecular dynamics (AIMD) simulations, time-dependent density functional theory (TDDFT) calculations, and transient absorption spectroscopy (TAS) analysis. Based on the experimental characterizations and previously reported studies,[37−39] Mn ions are incorporated by substituting Zn sites to form tetrahedral coordination with four surrounding anions. In this work, both InP and ZnSeS crystallize in the same space group ($F\bar{4}3m$) (Figure S2), which show closely matched lattice constants (InP: 5.9 Å; ZnSeS: 5.6 Å) with a theoretical lattice mismatch less than 5%, accounting for the low density of interfacial defects.[9] Building on these crystal structures, we investigated the electronic structure of the InP/ZnSeS interface model. As illustrated in Figure 2a, the calculated density of states (DOS) of the InP/ZnSeS heterostructure exhibits a distinct electronic state in the middle of the bandgap. Since the contributions from InP and ZnSeS are nearly identical (Figure S3), this feature can be attributed to the interfacial state caused by the hybridization between two components.[40] It is found that the conduction band (CB), as the main energy level range for hot electron transport, exhibits minimal variation between the InP and ZnSeS layers, which limits the efficient electron extraction in the InP/ZnSeS heterostructure. Therefore, modulating the CB to localize primarily within the ZnSeS region becomes a key objective of intraband regulation.

As displayed in Figure 2b, the DOS of the Mn-doped system shows that the Mn-induced electronic states are primarily distributed in the CB, which has negligible influence on the band gap and is consistent with the experimentally measured optical band gaps (Figure 1f,g). To understand how the intraband Mn doping states influence the hot electron's transport, we calculated the spatial distributions of electrons and holes in both undoped and Mn-doped systems, as presented in Figure 2c. In the undoped case, electrons and holes are similarly distributed in both the InP and ZnSeS layers. Such distribution leads to substantial electron−hole recombination, which is the primary reason for the low carrier extraction efficiency of this type of QDs.[41] After the incorporation of Mn atoms in the ZnSeS layer, the Mn-induced states (Figure 2b) become dominant at the conduction band minimum (CBM), thus causing electrons to accumulate predominantly in the ZnSeS layer, as indicated by the solid red lines in Figure 2c. Moreover, the hole density (dashed red line) in the ZnSeS layer also slightly increased, implying a potential improvement in the hole extraction efficiency.

We further calculated the band structure around the gamma point during the carrier dynamic process. Figure S4 demonstrates that the constructed InP/ZnSeS heterostructure model remains relatively stable at room temperature. As shown in Figure 2d,e, the energy fluctuations of each energy state within a 2000 fs time scale are presented for undoped and Mn-doped systems, respectively.[42−44] The relatively light coloration of the interfacial states indicates that the contributions from InP and ZnSeS are comparable and that the Mn doping does not significantly influence the interfacial states. However, Mn incorporation induces significant changes in the spatial distribution of the conduction and valence bands. In the undoped system (Figure 2d), the CB appears predominantly red, suggesting that electrons are mainly localized within the InP layer. After Mn doping, the CB near the CBM exhibits a clear blue color (Figure 2e), demonstrating that electrons preferentially accumulate in the ZnSeS layer during relaxation.

Figure 2f compares the transport directions of excited-state electrons within the CB of undoped and Mn-doped systems.[45] It can be observed that the excited electrons are mainly localized in the InP layer (corresponding to only 26% contribution from ZnSeS in Figure 2f) in the undoped system, whereas the electron distribution in the ZnSeS layer reaches up to 82% in the Mn-doped system. During the dynamic process, the electron distribution in the undoped system remains unchanged, while in the Mn-doped system, the hot electrons distinctly transport from InP to ZnSeS, with the proportion in the ZnSeS layer increasing from 66% to 82% at 300 fs. To better visualize the hot electron transfer process from InP to ZnSeS, we calculated the initial electron distribution at the CBM+0.6 eV energy level and the distribution after 1000 fs dynamics (0.6 eV was selected because electron transfer within this energy window shows clearly distinguishable differences). As shown in Figure 2g, the electrons initially concentrated in the InP layer gradually transport to the ZnSeS layer, with a predominant accumulation around Mn atoms, which confirms the role of Mn doping states in facilitating the electron aggregation. Indeed, the electron-collecting effect of Mn-induced doping states on hot electrons, as observed in molecular dynamics simulations, is also presented in the static partial charge density maps calculation of electrons and holes, as shown in Figures S5−S6, showing that the electrons are primarily distributed within the InP layer before Mn doping, while they localize around Mn atoms in the ZnSeS layer after Mn doping. Such transport mechanism of photogenerated electrons in the Mn-doped QDs is schematically illustrated in Figure 2h. Upon photoexcitation, electrons are first promoted to the CB as hot electrons.[46,47] In the undoped QDs, the photoexcited electrons undergoing relaxation are prone to recombine with holes in the InP core. In contrast, the hot electrons in the Mn-doped QDs migrate toward the CBM and accumulate around Mn atoms in the ZnSeS layer. Therefore, the Mn atoms can act as a 'bucket' that collect hot electrons to maintain the electron's distribution in the ZnSeS layer, thus facilitating the electron extraction from InP to the ZnSeS layer.

To verify the primary role of Mn-induced intraband doping states in influencing the hot electron transport in QDs, we

https://doi.org/10.1021/acsenergylett.6c00616
ACS Energy Lett. 2026, 11, 4465−4474

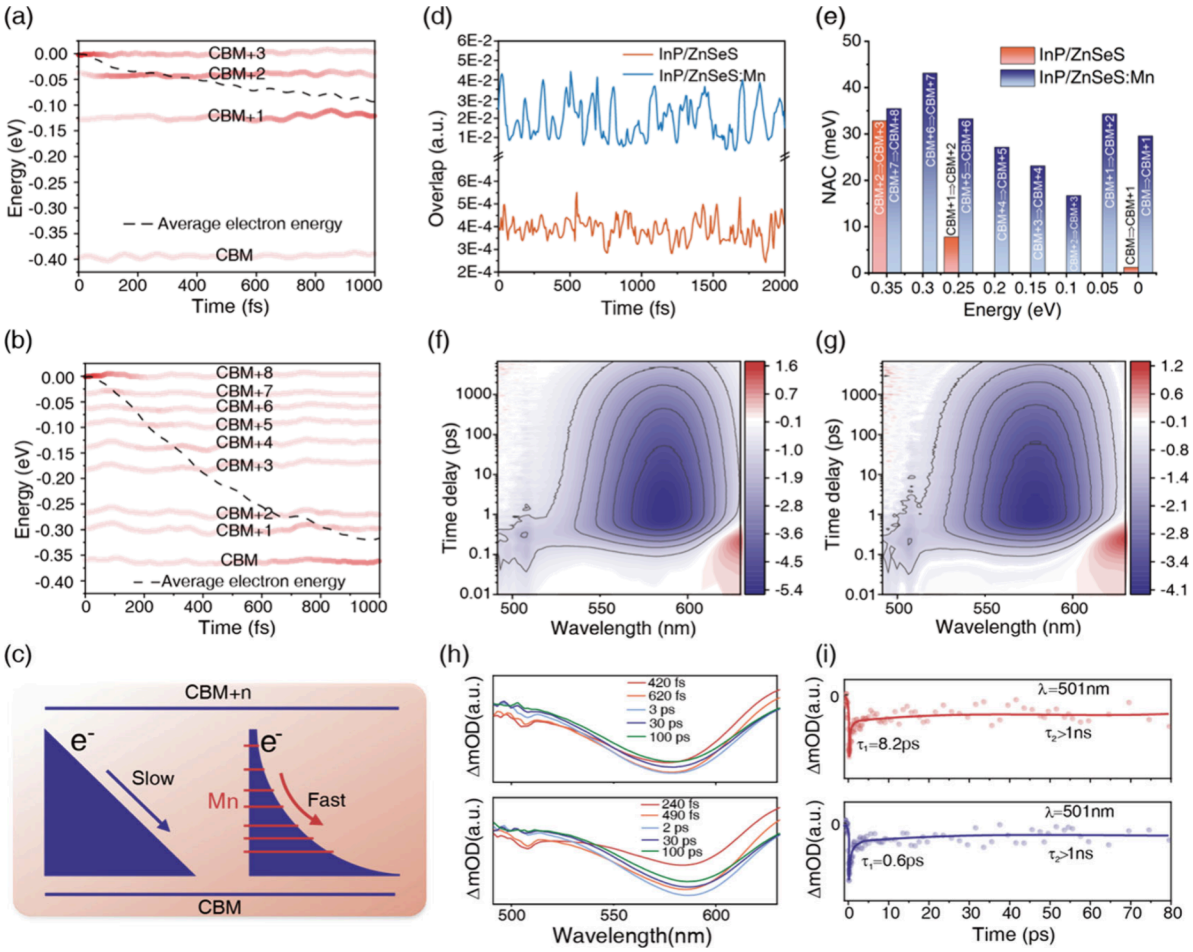

Figure 3. Time-dependent electron energy change for the (**a**) InP/ZnSeS and (**b**) InP/ZnSeS:Mn heterostructures. (**c**) Schematic diagram of the relaxation process of electrons from a photoexcited high-energy state to a low-energy state. The difference in electron relaxation pathways before and after Mn doping is a key factor to the significant variations in transport speed. (**d**) The average NAC of neighboring states in the CB for InP/ZnSeS (orange) and InP/ZnSeS:Mn (blue) obtained from molecular dynamics. For ease of comparison, the CBM was set to zero energy. (**e**) Time evolution of the wave function overlap between adjacent states in the CB of InP/ZnSeS and InP/ZnSeS:Mn heterostructures. Pseudocolor TAS plots and temporal evolution spectra of (**f**) InP/ZnSeS and (**g**) InP/ZnSeS:Mn QDs (Average pump fluence of 6 μJ/cm^2). (**h**) Ultrafast time-resolved TA spectra of InP/ZnSeS (up) and InP/ZnSeS:Mn (down) QDs. (**i**) Dynamics at probe wavelengths of 501 nm for InP/ZnSeS (red) and InP/ZnSeS:Mn (blue) QDs, respectively.

further calculated the dynamics of carriers at various stages during transport processes. As shown in Figure S7, the electron−hole recombination time was computed via TDDFT and the simulated recombination times exhibit no significant change upon Mn doping, which is in good agreement with the experimentally measured carrier lifetimes from PL and TAS spectra (Table S2, Figure S8, and Figure S9), indicating that Mn incorporation exerts a negligible influence on the electron−hole recombination.[48−51] Hence, we further primarily focus on the impact of Mn-induced intraband states within the CB on the hot electron transport dynamics.[44,52]

We then calculated the hot electron transport processes in both undoped and Mn-doped systems,[42] as shown in Figure 3a,b. It can be observed that within 1000 fs, the electron transfer in the CB proceeds relatively slowly in the undoped system, whereas the electrons in the Mn-doped system rapidly transfer to the CBM. The schematic diagram in Figure 3c illustrates the distinct hot electron transport pathways in the undoped and Mn-doped systems. For the undoped system, hot electrons exhibit a slower transportation toward the CBM, while the Mn-doping states provide a more efficient transport pathway for hot electron relaxation. To further investigate the acceleration mechanism of electron transfer in the Mn-doped system, we studied the role of electron−phonon coupling in hot electron transportation. Here, electron−phonon coupling is treated as nonadiabatic coupling (NAC),[53−55] and the expression for NAC is provided as follows:[56−58]

$$\boldsymbol{d}_{jk} = \left\langle \phi_j \middle| \frac{\partial}{\partial t} \middle| \phi_k \right\rangle = \sum_I \frac{\langle \phi_j | \nabla_{R_I} \hat{H} | \phi_k \rangle}{\varepsilon_k - \varepsilon_j} \cdot \boldsymbol{R}_I$$

Here, $\hat{H}$ represents the Kohn−Sham Hamiltonian; ϕ_j, ϕ_k, ε_j, and ε_k denote the wave functions and eigenvalues of electronic states j and k, respectively; $\boldsymbol{R}_I$ is the nuclear velocity term.[59,60] As shown in the formula, the coupling primarily depends on the wave functions overlap and energy gap.[61−63]

As observed in Figure 3a, a substantial energy gap exists between the CBM and CBM+1 in the undoped system, which results in a weaker electron−phonon coupling and constitutes the primary cause of slow carrier transport. Upon Mn doping, the introduced doping states further fill this energy gap to reduce the energy difference and enhance the electron−phonon coupling for the consequently accelerated transfer process.[43,44] Since the formula highlights the significance of

https://doi.org/10.1021/acsenergylett.6c00616
ACS Energy Lett. 2026, 11, 4465−4474

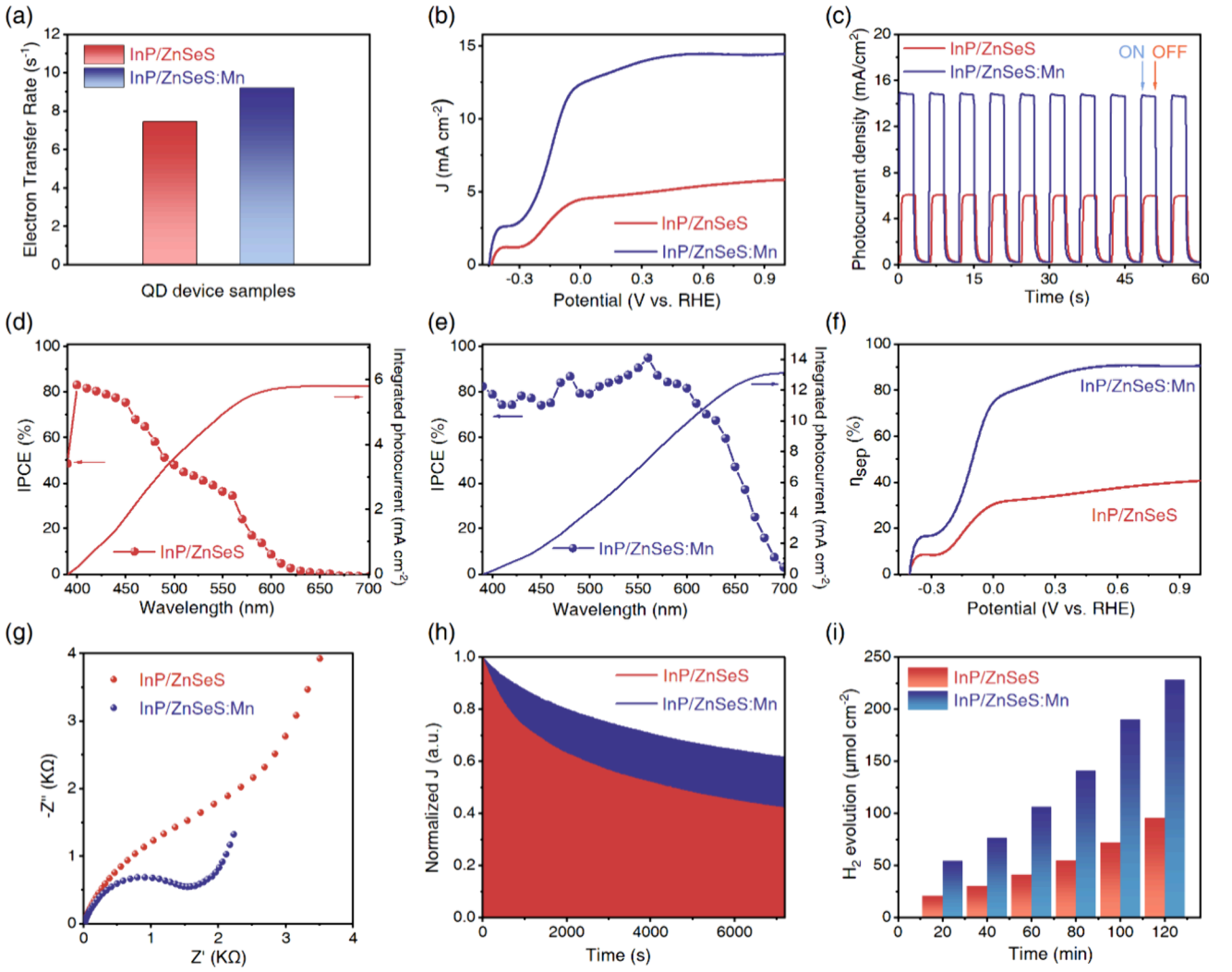

Figure 4. (**a**) The calculated electron transfer rates, (**b**) *J*−*V* curves under illumination (1 sun, AM 1.5G, 100 mW cm^{-2}), and (**c**) *J*-*t* curves under chopped illumination at an applied bias of 0.4 V (vs RHE) for InP/ZnSeS and InP/ZnSeS:Mn QDs-based PEC devices. IPCE spectra of (**d**) InP/ZnSeS and (**e**) InP/ZnSeS:Mn QDs-based PEC cells. (**f**) The calculated carrier separation efficiency, (**g**) EIS Nyquist plots, (**h**) normalized photocurrent density versus time at 0.4 V vs RHE for 2 h testing, and (**i**) experimental H_2 evolution rates for 2 h illumination under applied bias of 0.4 V vs RHE for two types of QDs-based PEC devices.

wave function overlap,[55] we also calculated the wave function overlap between two adjacent states (CBM+3 and CBM+2 for undoped system and CBM+8 and CBM+7 for doped system, respectively) within the CB (Figure 3d). During the dynamic process, the wave function overlap exhibits an order of magnitude increase after Mn doping, which is another key factor to strengthen the electron−phonon coupling (Figure 3e). Therefore, Mn doping creates a high-speed channel for hot electron transfer from InP to the ZnSeS layer, thus significantly improving the electron extraction efficiency of InP/ZnSeS QDs.

Based on the calculated acceleration effect of Mn doping states on hot electron transport, we further performed the experimental TAS characterization on undoped and Mn-doped QDs under 405 nm pump excitation at representative delay times, as shown in Figure 3f,g. The pseudocolor TAS plots of both samples exhibit similar spectral features with a significant negative absorption peak around 580 nm, which corresponds to the absorption peak in Figure 1f that originates from the ground-state bleaching (GSB) due to electron filling of the band-edge states.[64−66] Moreover, a weaker bleaching peak appears at a higher energy of 507 nm in both samples (Figure 3h), which is ascribed to the bleaching induced by the transition of higher energy levels in the CB.[65,66] To clarify the acceleration of hot electron transport, we further consider fitting the decay kinetics of the signal at 501 nm (near 507 nm),[65,66] as shown in Figure 3i. As compared to the fast time component of 8.2 ps in undoped QDs, the fast time component of Mn-doped QDs is dramatically accelerated to an ultrafast time scale of 600 fs, which is consistent with the trend of theoretical calculations presented in Figure 3a,b. Theoretical results (Figure 2) further reveal that this acceleration originates from the Mn doping states, which provide a more efficient transport pathway for hot electron relaxation (Figure 3c). These findings indicate that Mn-doped QDs can realize efficient hot electron extraction by regulating hot electron transport within the conduction band. In addition to the physical mechanism discussed above, other previously proposed mechanisms also play a role in enhancing the photoelectron extraction. For instance, as shown in Figure S10 and Figure S11, the undoped QDs exhibit no spin polarization and indicate that electrons with opposite spins occupy

https://doi.org/10.1021/acsenergylett.6c00616
ACS Energy Lett. 2026, 11, 4465−4474

equivalent orbitals. In contrast, the Mn-doped QDs display distinct spin polarization, and thereby the spin-flip process must be considered during the electron relaxation, which reduces the possibility of electron−hole recombination for a more efficient carrier extraction (Figure S12).[67,68] We also calculated the carrier concentration distribution, and the results in Figure S13 show a significant increase in carrier concentration and conductivity near the CB after Mn doping.

To experimentally verify the positive role of hot electron transport in Mn-doped InP/ZnSeS QDs, we fabricated the QD-based PEC devices and evaluated their performance using a standard three-electrode PEC system (Figure S14).[20,69] As shown in Figure S15, the photocurrent densities of QD-based PEC devices with varying Mn doping concentrations (atomic ratios of 15.1%, 19.2%, and 26.9%) were first measured to determine the optimized Mn doping level, wherein the PEC device based on QDs with a Mn doping ratio of 19.2% exhibited the highest photocurrent density, while the QD-PEC device with a Mn doping ratio of 26.9% showed a cliff-like decline. This reduced photocurrent density of the QDs-PEC device with excessive Mn doping level could be attributed to the lattice distortion within the QDs[6] for a deteriorated carrier dynamics. Figure S16 depicts the light absorption measurements of the QDs-PEC devices with different Mn doping concentrations, in which the light absorbance of these QD-device samples increased from Mn doping level of 15.1% to 19.2%, while the device sample with Mn doping concentration of 26.9% showed a significantly decreased photocurrent density, which is consistent with the trend observed in Figure S15.

As shown in Figure S17 and Figure 4a, we first calculated the electron transfer rate of these QDs-based photoelectrodes by measuring the PL decay curves of QDs deposited on TiO_2 and ZrO_2 electrodes, respectively.[34] The electron transfer rate of an InP/ZnSeS:Mn QDs-based photoelectrode shows a clear improvement with respect to that of the undoped InP/ZnSeS QDs-based sample, which is similar to the increasing trend of the calculated hole transfer rate, as summarized in Table S3. As demonstrated in Figure 4b, under standard 1 sun illumination (AM 1.5G, 100 mW cm^{-2}), the incorporation of Mn into InP/ZnSeS QDs leads to a significant increase in the photocurrent density of as-fabricated QDs-based PEC devices, reaching up to 14.6 mA/cm^2 that represents a state-of-the-art performance among various eco-friendly QDs-based PEC devices (summarized in Table S4 and Figure S18). Additionally, as exhibited in Figure 4c, the transient photocurrent response of these QDs-based PEC cells measured under chopped illumination shows a stable photoresponse that is consistent with the $J-V$ curves (Figure 4b).

Figure 4d,e shows the incident photon-to-electron conversion efficiency (IPCE) spectra of these QD-based PEC devices. As compared to the undoped InP/ZnSeS QDs-based device sample, the InP/ZnSeS:Mn QDs-based PEC device exhibits enhanced IPCE values over a broad wavelength range (400−700 nm), indicating a higher photon-to-electron conversion efficiency that is consistent with the enhanced photogenerated electron distribution in the ZnSeS layer of Mn-doped InP/ZnSeS QDs for a higher carrier extraction efficiency. Besides, the calculated integrated photocurrent densities for the InP/ZnSeS and InP/ZnSeS:Mn QDs-PEC cells are approximately 5.8 mA cm^{-2} and 13.1 mA cm^{-2}, which align well with the photocurrent densities obtained from the $J-V$ curves (Figure 4b). To further understand the effect of Mn doping on the performance of QDs-PEC devices, we examined the charge separation efficiency (η_{sep}) as a function of the applied potential (Figure 4f). Herein, the η_{sep} was estimated using the equation $J_{ph} = J_{abs} \times \eta_{sep} \times \eta_{transfer}$, where J_{ph} is the measured photocurrent density, J_{abs} is the theoretical photocurrent density, and $\eta_{transfer}$ is the carrier transfer efficiency.[19,70] When an effective hole scavenger (Na_2S/Na_2SO_3 in this work) is added to the electrolyte solution, the carrier transfer efficiency can be assumed to be nearly 100% ($\eta_{transfer} \approx 1$), and the η_{sep} can be approximated as J_{ph}/J_{abs}.[19] As shown in Figure 4f, the Mn-doped QDs-based PEC device achieved a significant enhancement in η_{sep} compared to the undoped QDs-based device sample, which is in agreement with our theoretical prediction showing that the Mn-related intraband states could enhance the electron accumulation in the ZnSeS layer of QDs, thus leading to the efficient charge extraction/separation in the QDs-PEC cells.[19] In addition, we investigated the charge kinetics of both types of QDs-based photoanodes using electrochemical impedance spectroscopy (EIS), as shown in Figure 4g. The smaller semicircular diameter observed for the InP/ZnSeS:Mn QDs-based PEC device indicates a lower charge transfer resistance, representing the improved interface charge transfer characteristics induced by the enhanced photogenerated electron distribution in the InP/ZnSeS QDs after Mn doping. We also measured the *J-t* curves of two QDs-PEC devices to assess their long-term stability. As shown in Figure 4h, the InP/ZnSeS QDs-based device retained only about 40% of its initial activity after 2 h of continuous light irradiation. In contrast, the InP/ZnSeS:Mn QDs-based PEC device showed an improved stability, maintaining 63% of its initial activity after 2 h of continuous illumination. Such enhanced device stability is attributed to the optimized overall charge carrier dynamics in the Mn-doped QDs-based PEC cell.[4,20] Moreover, the H_2 production rates for InP/ZnSeS and InP/ZnSeS:Mn QDs-based PEC devices were measured to be 45 μmol cm^{-2} h^{-1} and 117 μmol cm^{-2} h^{-1}, respectively (Figure 4i), further confirming that our intraband regulation through Mn doping significantly promotes the carrier extraction efficiency in InP/ZnSeS QDs to realize efficient PEC hydrogen evolution.

In summary, this work elucidates the modulation of hot electron transport in environment-friendly InP/ZnSeS QDs via Mn doping to achieve high-efficiency solar-driven QDs-based PEC devices. It is demonstrated that the Mn incorporation in ZnSeS introduces new transport pathways within the QDs, enabling efficient and directional transfer of hot electrons from the InP core to the ZnSeS shell. TAS analysis confirmed the Mn doping-induced new transport channels could significantly accelerate the hot electron transfer by nearly an order of magnitude. As compared to the pristine InP/ZnSeS QDs, this Mn-doping modulation of hot electron transport enables the rapid separation of electrons and holes immediately after photoexcitation of InP/ZnSeS:Mn QDs, thereby significantly enhancing the carrier extraction efficiency. As a result, an as-fabricated InP/ZnSeS:Mn QDs-based PEC cell delivers a saturated photocurrent density of 14.6 mA cm^{-2} under standard 1 sun illumination (AM 1.5G, 100 mW cm^{-2}), representing a state-of-the-art performance among the best reported heavy-metal-free QDs-based PEC devices. This hot electron regulation strategy provides a viable paradigm for overcoming the intrinsic carrier confinement limitation in type-I core/shell QDs, opening new opportunities for advancing

https://doi.org/10.1021/acsenergylett.6c00616
ACS Energy Lett. 2026, 11, 4465−4474

cost-effective, eco-friendly, and highly efficient QDs-based solar energy conversion technologies.

■ ASSOCIATED CONTENT

Supporting Information

The Supporting Information is available free of charge at https://pubs.acs.org/doi/10.1021/acsenergylett.6c00616.

ICP-OES elemental analysis, average lifetime and fitting parameters, calculated photogenerated electron/hole transfer rates, comparison of photocurrent density, HRXPS spectra, crystal model used for constructing the heterojunction, contributions of different components to the interfacial states in the DOS, the energy changes during the simulated dynamics process, electron distributions by static calculation, hole distributions by static calculation, simulated electron−hole recombination time, time-resolved PL spectra, TAS dynamics, band structure with spin polarization, DOS with spin polarization, schematic diagram of hot-electron relaxation process with spin flip, calculated carrier concentration and conductivity, schematic of the QDs-PEC device, J-V curves, UV−vis absorption spectra of QDs-PEC devices, time-resolved PL spectra used for calculating carrier transport rate, PEC performance comparison with other eco-friendly QDs-based systems (PDF)

■ AUTHOR INFORMATION

Corresponding Authors

Xin Tong − *Institute of Fundamental and Frontier Sciences, University of Electronic Science and Technology of Chin, Chengdu 611731, P. R. China;* orcid.org/0000-0001-6066-056X; Email: xin.tong@uestc.edu.cn

Alexander O. Govorov − *Institute of Fundamental and Frontier Sciences, University of Electronic Science and Technology of Chin, Chengdu 611731, P. R. China;* orcid.org/0000-0003-1316-6758; Email: govorov@ohio.edu

Mengyan Dai − *State Key Laboratory of Chemistry for NBC Hazards Protection, Beijing 102205, P. R. China;* Email: daidecai0558@163.com

Zhiming M. Wang − *Institute of Fundamental and Frontier Sciences, University of Electronic Science and Technology of Chin, Chengdu 611731, P. R. China; School of Physics, University of Electronic Science and Technology of China, Chengdu 611731, P. R. China;* orcid.org/0000-0001-7847-7704; Email: zhmwang@uestc.edu.cn

Authors

Yisen Yao − *Institute of Fundamental and Frontier Sciences, University of Electronic Science and Technology of Chin, Chengdu 611731, P. R. China;* orcid.org/0000-0002-4045-6649

Guohua Mi − *Institute of Fundamental and Frontier Sciences, University of Electronic Science and Technology of Chin, Chengdu 611731, P. R. China*

Guoqi Xiang − *Solar Energy Integration Technology Popularization and Application Key Laboratory of Sichuan Province, Panzhihua University, Panzhihua 617000, P. R. China*

Xin Li − *Solar Energy Integration Technology Popularization and Application Key Laboratory of Sichuan Province, Panzhihua University, Panzhihua 617000, P. R. China*

Fan Cui − *School of Physics, University of Electronic Science and Technology of China, Chengdu 611731, P. R. China*

Ziyao Xiong − *Institute of Fundamental and Frontier Sciences, University of Electronic Science and Technology of Chin, Chengdu 611731, P. R. China; State Key Laboratory of Chemistry for NBC Hazards Protection, Beijing 102205, P. R. China*

Wuyang Ren − *Institute of Fundamental and Frontier Sciences, University of Electronic Science and Technology of Chin, Chengdu 611731, P. R. China*

Complete contact information is available at: https://pubs.acs.org/10.1021/acsenergylett.6c00616

Author Contributions

⊥(Y.Y., G.M.) These authors contributed equally to this work.

Notes

The authors declare no competing financial interest.

■ ACKNOWLEDGMENTS

All authors would like to thank Professor Arup Neogi and Dr. Chengjie Wang for their assistance with the TAS measurements. X.T. acknowledges the support from Sichuan Science and Technology Program (No. 2025JDRC0001). X.T. and X.L. acknowledge the support from Solar Energy Integration Technology Popularization and Application Key Laboratory of Sichuan Province (No. 25TYNJS-Z-01, 25TYNJS-Z-04). Y.Y. acknowledges the support from China Postdoctoral Science Foundation (No. 2024M750338) and Postdoctoral Fellowship program (Grade C) of China Postdoctoral Science Foundation (No. GZC20240214). Z.M.W. acknowledges the support from "111 Project" (No. B20030).

■ REFERENCES

(1) García de Arquer, F. P.; Talapin, D. V.; Klimov, V. I.; Arakawa, Y.; Bayer, M.; Sargent, E. H. Semiconductor quantum dots: Technological progress and future challenges. *Science* **2021**, *373* (6555), No. eaaz8541.

(2) Kagan, C. R.; Lifshitz, E.; Sargent, E. H.; Talapin, D. V. Building devices from colloidal quantum dots. *Science* **2016**, *353* (6302), aac5523.

(3) Kwak, D. H.; Ramasamy, P.; Lee, Y. S.; Jeong, M. H.; Lee, J. S. High-Performance Hybrid InP QDs/Black Phosphorus Photodetector. *ACS Appl. Mater. Interfaces* **2019**, *11* (32), 29041−29046.

(4) Mi, G. H.; Yao, Y. S.; Xia, L.; Zhao, H. Y.; Yang, Q.; Wang, Z. M. M.; Tong, X. Reinforcing Photogenerated Carrier Extraction of Environment-Friendly InP/ZnSeS Quantum Dots for High-Performing Photoelectrochemical Photodetection and Solar Energy Conversion. *Small* **2025**, *21* (2), 11.

(5) Luo, B.; Liu, J. B.; Guo, H.; Liu, X.; Song, R.; Shen, K.; Wang, Z. M. M.; Jing, D. W.; Selopal, G. S.; Rosei, F. High efficiency photoelectrochemical hydrogen generation using eco-friendly Cu doped Zn-In-Se colloidal quantum dots. *Nano Energy* **2021**, *88*, 106220.

(6) Zhao, H. Y.; Li, X.; Cai, M. K.; Liu, C.; You, Y. M.; Wang, R.; Channa, A. I.; Lin, F.; Huo, D.; Xu, G. F.; Tong, X.; Wang, Z. M. Role of Copper Doping in Heavy Metal-Free InP/ZnSe Core/Shell Quantum Dots for Highly Efficient and Stable Photoelectrochemical Cell. *Adv. Energy Mater.* **2021**, *11* (31), 10.

(7) Jin, L.; Selopal, G. S.; Tong, X.; Perepichka, D. F.; Wang, Z. M. M.; Rosei, F. Heavy-Metal-Free Colloidal Quantum Dots: Progress

and Opportunities in Solar Technologies. *Adv. Mater.* **2024**, *36* (33), 31.
(8) Won, Y. H.; Cho, O.; Kim, T.; Chung, D. Y.; Kim, T.; Chung, H.; Jang, H.; Lee, J.; Kim, D.; Jang, E. Highly efficient and stable InP/ZnSe/ZnS quantum dot light-emitting diodes. *Nature* **2019**, *575* (7784), 634.
(9) Baek, H.; Kang, S.; Heo, J.; Choi, S.; Kim, R.; Kim, K.; Ahn, N.; Yoon, Y.-G.; Lee, T.; Chang, J. B.; Lee, K. S.; Park, Y.-G.; Park, J. Insights into structural defect formation in individual InP/ZnSe/ZnS quantum dots under UV oxidation. *Nat. Commun.* **2024**, *15* (1), 1671.
(10) Hughes, K. E.; Stein, J. L.; Friedfeld, M. R.; Cossairt, B. M.; Gamelin, D. R. Effects of Surface Chemistry on the Photophysics of Colloidal InP Nanocrystals. *ACS Nano* **2019**, *13* (12), 14198−14207.
(11) Rajan, D.; Manoj, B.; Krishna, S.; Thomas, A.; Thomas, K. G. The Rise of InP Quantum Dots in Nanoscience. *ACS Energy Lett.* **2025**, *10* (8), 3700−3728.
(12) Chen, Y.; Wei, Q.; Fu, J.; Lin, S.; Ren, H.; Liu, Q.; Zhou, L.; Yin, J.; Li, M. Hot-Electron Extraction from Perovskite Quantum Dots for Photovoltage Enhancement. *ACS Energy Lett.* **2025**, *10* (11), 5439−5446.
(13) Bian, Y.; Yan, X.; Chen, F.; Li, Q.; Li, B.; Hou, W.; Lu, Z.; Wang, S.; Zhang, H.; Zhang, W.; Zhang, D.; Tang, A.; Fan, F.; Shen, H. Efficient green InP-based QD-LED by controlling electron injection and leakage. *Nature* **2024**, *635* (8040), 854−859.
(14) Luo, J. Y.; Tong, X.; Yue, S.; Wu, K. M.; Li, X.; Zhao, H. Y.; Wang, B. Y.; Li, Z. J.; Liu, X. F.; Wang, Z. M. Tailored Environment-Friendly Reverse Type-I Colloidal Quantum Dots for a Near-Infrared Optical Synapse and Artificial Vision System. *ACS Nano* **2024**, *18* (43), 29991−30003.
(15) Hu, H.; Wen, G. H.; Wen, J. M.; Huang, L. B.; Zhao, M.; Wu, H. L.; Sun, Z. H. Ambipolar Charge Storage in Type-I Core/Shell Semiconductor Quantum Dots toward Optoelectronic Transistor-Based Memories. *Adv. Sci.* **2021**, *8* (16), 9.
(16) Grimaldi, G.; Crisp, R. W.; ten Brinck, S.; Zapata, F.; van Ouwendorp, M.; Renaud, N.; Kirkwood, N.; Evers, W. H.; Kinge, S.; Infante, I.; Siebbeles, L. D. A.; Houtepen, A. J. Hot-electron transfer in quantum-dot heterojunction films. *Nat. Commun.* **2018**, *9*, 10.
(17) Yu, S.; Fan, X.-B.; Wang, X.; Li, J.; Zhang, Q.; Xia, A.; Wei, S.; Wu, L.-Z.; Zhou, Y.; Patzke, G. R. Efficient photocatalytic hydrogen evolution with ligand engineered all-inorganic InP and InP/ZnS colloidal quantum dots. *Nat. Commun.* **2018**, *9* (1), 4009.
(18) Liu, J.; Yue, S.; Zhang, H.; Wang, C.; Barba, D.; Vidal, F.; Sun, S.; Wang, Z. M.; Bao, J.; Zhao, H.; Selopal, G. S.; Rosei, F. Efficient Photoelectrochemical Hydrogen Generation Using Eco-Friendly "Giant" InP/ZnSe Core/Shell Quantum Dots. *ACS Appl. Mater. Interfaces* **2023**, *15* (29), 34797−34808.
(19) Zheng, Q.; Wang, J.; Huang, F.; Huang, Z.; Tian, S.; Chen, Q.; Pei, Y.; Zheng, K.; Tian, J. Constructing InP/ZnSe Quantum Dots with Shell Gradient In^{3+} Doping for Photoelectrochemical Cells. *ACS Energy Lett.* **2024**, *9* (5), 2358−2366.
(20) Mi, G.; Yao, Y.; Yang, Q.; Wang, L.; Li, X.; Xia, L.; Long, Z.; Yang, D.; Wang, Z.; Tong, X. Synergistic Surface Under-Coordinated Sites and Ligand Engineering of Colloidal Quantum Dots for High-Efficiency Bifunctional Photoelectrochemical Devices. *Adv. Funct. Mater.* **2026**, *36* (14), No. e20672.
(21) Jana, S.; Srivastava, B. B.; Jana, S.; Bose, R.; Pradhan, N. Multifunctional Doped Semiconductor Nanocrystals. *J. Phys. Chem. Lett.* **2012**, *3* (18), 2535−2540.
(22) Gi, E.; Jiang, B.; Liu, K.; Olshansky, J. H. Temperature-dependent energy transfer dynamics in InP/$Mn_xZn_{1-x}S$ core/shell quantum dots. *J. Inf. Dispersion* **2025**, *26* (2), 65−73.
(23) Rabouw, F. T.; Vaxenburg, R.; Bakulin, A. A.; van Dijk-Moes, R. J. A.; Bakker, H. J.; Rodina, A.; Lifshitz, E.; Efros, A. L.; Koenderink, A. F.; Vanmaekelbergh, D. Dynamics of Intraband and Interband Auger Processes in Colloidal Core-Shell Quantum Dots. *ACS Nano* **2015**, *9* (10), 10366−10376.
(24) He, Y.; Zhao, Y.; Wang, X.; Liu, Z.; Yu, Y.; Li, L. Multiple Heteroatom-Hydrogen Bonds Bridging Electron Transport in Covalent Organic Framework-Based Supramolecular System for Photoreduction of CO_2. *Angew. Chem.-Int. Ed.* **2023**, *62* (31), No. e202307160.
(25) Zhang, J.; Li, J.; Ye, Z.; Cui, J.; Peng, X. Hot-Electron-Induced Photochemical Properties of CdSe/ZnSe Core/Shell Quantum Dots under an Ambient Environment. *J. Am. Chem. Soc.* **2023**, *145* (25), 13938−13949.
(26) Feng, J. N.; Fan, K. Z.; Cao, Q. X.; Liang, W. F.; Wong, P. Y.; Xue, J.; Chang, K. T.; Wong, K. S.; Lu, H. P. Hot Electron Photocatalysis Using Nontoxic Self-Doped Quantum Dots. *Angew. Chem.-Int. Ed.* **2025**, *64* (45), 9.
(27) Vonk, S. J. W.; Prins, P. T.; Wang, T.; Matthys, J.; Giordano, L.; Schiettecatte, P.; Mondal, N.; Geuchies, J. J.; Houtepen, A. J.; van der Hoeven, J. E. S.; Hopper, T. R.; Hens, Z.; Geiregat, P.; Bakulin, A. A.; Rabouw, F. T. Hot-carrier trapping preserves high quantum yields but limits optical gain in InP-based quantum dots. *Nat. Commun.* **2025**, *16* (1), 6249.
(28) Dong, Y.; Choi, J.; Jeong, H.-K.; Son, D. H. Hot Electrons Generated from Doped Quantum Dots via Upconversion of Excitons to Hot Charge Carriers for Enhanced Photocatalysis. *J. Am. Chem. Soc.* **2015**, *137* (16), 5549−5554.
(29) Orrison, C.; Schulze, I. C.; Zhang, Z.; Freitas, D.; Murray, I.; Yan, X.; Hilty, C.; Son, D. H. Determination of the Generation Efficiency and Reductive Reactivity of the Upconverted Hot Electrons from Mn-Doped Quantum Dots under Weak Visible Light. *J. Am. Chem. Soc.* **2025**, *147* (41), 37497−37505.
(30) Cao, Q.; Feng, J.; Fan, K.; Zhang, S.; Zhang, J.; Ma, B.; Xue, J.; Li, X.; Wang, K.; Tao, L.; Sergeev, A.; Yang, Y.; Wong, K. S.; Huang, Y.; Lu, H. Extreme Potential Photocatalysis Enabled by Spin-exchange Auger Processes in Magnetic-doped Quantum Dots. *Nat. Commun.* **2025**, *16* (1), 5280.
(31) Huang, P.; Wang, L.; Bai, T.; Lv, Y.; Zhu, J.; Liu, F.; Li, H.; Wu, K. Spin-Exchange Interaction in Mn^{2+}-Doped InP Colloidal Quantum Dots Revealed through Correlated Magneto-Optical Spectroscopy and Transient Carrier Dynamics. *Nano Lett.* **2026**, *26* (1), 552−559.
(32) Yuan, S.; Zheng, Y.; Chu, Y.; Xia, C.; Dong, R.; Xu, J.; Teng, B.; Wu, Y.; He, Y. Cu doping induced lattice distortion and oxygen vacancy formation in $PbBiO_2Br$: Band structure modulation enhances photocatalytic nitrogen fixation and pollutant degradation performance. *Green Energy Environ.* **2026**, *11*, 211.
(33) Okamoto, A.; Toda, S.; Tsujihata, T.; Kamada, T.; Huang, M.; Hashimoto, Y.; Isojima, S.; Kajii, H.; Seino, S.; Kurashiki, T. Enhanced Optical Properties of Green-Emitting InP Quantum Dots with Matched Junctions of the Core and Mn-Doped Novel Shells. *Adv. Mater. Interfaces* **2025**, *12* (7), 9.
(34) Yang, Q.; Tong, X.; Zhao, H. Y.; Mi, G. H.; Gu, L. P.; Xia, L.; Wang, Z. M. Spin-polarized colloidal quantum dots for highly efficient magnetic field-assisted photoelectrochemical solar energy conversion. *Appl. Catal. B-Environ. Energy* **2025**, *368*, 125132.
(35) Pradhan, N.; Sarma, D. D. Advances in Light-Emitting Doped Semiconductor Nanocrystals. *J. Phys. Chem. Lett.* **2011**, *2* (21), 2818−2826.
(36) Guo, R. Q.; Meng, J.; Lin, W. H.; Liu, A. Q.; Pullerits, T.; Zheng, K. B.; Tian, J. J. Manganese doped eco-friendly $CuInSe_2$ colloidal quantum dots for boosting near-infrared photodetection performance. *Chem. Eng. J.* **2021**, *403*, 126452.
(37) Norris, D. J.; Yao, N.; Charnock, F. T.; Kennedy, T. A. High-quality manganese-doped ZnSe nanocrystals. *Nano Lett.* **2001**, *1* (1), 3−7.
(38) Liang, Y. F.; Yang, Y. P.; Wang, J. B.; Cheng, X. R.; Yuan, C. S.; Zhu, X.; Xie, H.; Wang, Z.; Li, H. N.; Feng, S. Q. Pressure-Induced Irreversible Metallization Accompanying Phase Transition of Chalcopyrite $Cu(In_{0.7}Ga_{0.3})Se_2$. *Inorg. Chem.* **2024**, *63* (31), 14623−14629.
(39) Lee, H. J.; Im, S.; Jung, D. J.; Kim, K.; Chae, J. A.; Lim, J.; Park, J. W.; Shin, D.; Char, K.; Jeong, B. G.; Park, J. S.; Hwang, E.; Lee, D.; Park, Y. S.; Song, H. J.; Chang, J. H.; Bae, W. K. Coherent Heteroepitaxial Growth of I-III-VI_2 $Ag(In,Ga)S_2$ Colloidal Nanocrystals with Near-unity Quantum Yield for Use in Luminescent Solar

https://doi.org/10.1021/acsenergylett.6c00616
ACS Energy Lett. 2026, 11, 4465−4474

Concentrators. *Nat. Commun.* **2023**, *14* (1). DOI: 10.1038/s41467-023-39509-y.
(40) Shi, X. W.; Dai, C.; Wang, X.; Hu, J. Y.; Zhang, J. Y.; Zheng, L. X.; Mao, L.; Zheng, H. J.; Zhu, M. S. Protruding Pt single-sites on hexagonal $ZnIn_2S_4$ to accelerate photocatalytic hydrogen evolution. *Nat. Commun.* **2022**, *13* (1), 10.
(41) Peng, M. F.; Tao, Y.; Bao, D. Q.; Wang, K. H.; Sun, X. H. Rational Synthesis of Core/shell Heterostructured Quantum Dots for Improved Self-powered Photodetection Performance Enabled by Energy Band Engineering. *Nano Energy* **2024**, *129*, 110033.
(42) Zheng, Q. J.; Saidi, W. A.; Xie, Y.; Lan, Z. G.; Prezhdo, O. V.; Petek, H.; Zhao, J. Phonon-Assisted Ultrafast Charge Transfer at van der Waals Heterostructure Interface. *Nano Lett.* **2017**, *17* (10), 6435−6442.
(43) Chu, W. B.; Tan, S. J.; Zheng, Q. J.; Fang, W.; Feng, Y. X.; Prezhdo, O.; Wang, B.; Li, X. Z.; Zhao, J. Ultrafast Charge Transfer Coupled to Quantum Proton Motion at Molecule/metal Oxide Interface. *Sci. Adv.* **2022**, *8* (24), 9.
(44) Chu, W. B.; Saidi, W. A.; Zhao, J.; Prezhdo, O. V. Soft Lattice and Defect Covalency Rationalize Tolerance of β-$CsPbI_3$ Perovskite Solar Cells to Native Defects. *Angew. Chem.-Int. Ed.* **2020**, *59* (16), 6435−6441.
(45) Low, P. J.; Chu, W.; Nie, Z.; Bin Mohd Yusof, M. S.; Prezhdo, O. V.; Loh, Z.-H. Observation of a transient intermediate in the ultrafast relaxation dynamics of the excess electron in strong-field-ionized liquid water. *Nat. Commun.* **2022**, *13* (1), 9.
(46) Pan, Z. W.; Zhu, X.; Liu, Y. X.; Yang, L.; Jiao, M. Y.; Kang, S.; Luo, J. L.; Fu, X.; Lu, W. Q. Enhanced Light Absorption and Photo-Generated Charge Separation Efficiency for Boosting Photocatalytic H_2 Evolution through TiO_2 Quantum Dots with N-Doping and Concomitant Oxygen Vacancy. *Small* **2024**, *20* (36), 11.
(47) Geng, W. T.; Liu, Y. C.; Xu, N.; Tang, G.; Kawazoe, Y.; Wang, V. Empowering materials science with VASPKIT: A Toolkit for Enhanced Simulation and Analysis. *Nat. Protoc.* **2025**, *20*, 3143.
(48) Yuan, Y.; Yan, G. H.; Dreessen, C.; Rudolph, T.; Huelsbeck, M.; Klingebiel, B.; Ye, J. J.; Rau, U.; Kirchartz, T. Shallow Defects and Variable Photoluminescence Decay Times up to 280 μs in Triple-cation Perovskites. *Nat. Mater.* **2024**, *23* (3), 391.
(49) Yuan, Y.; Yan, G. H.; Dreessen, C.; Kirchartz, T. Understanding Power-Law Photoluminescence Decays and Bimolecular Recombination in Lead-Halide Perovskites. *Adv. Energy Mater.* **2025**, *15* (6), 13.
(50) Krückemeier, L.; Krogmeier, B.; Liu, Z. F.; Rau, U.; Kirchartz, T. Understanding Transient Photoluminescence in Halide Perovskite Layer Stacks and Solar Cells. *Adv. Energy Mater.* **2021**, *11* (19), 19.
(51) Al-Ashouri, A.; Kohnen, E.; Li, B.; Magomedov, A.; Hempel, H.; Caprioglio, P.; Marquez, J. A.; Morales Vilches, A. B.; Kasparavicius, E.; Smith, J. A.; Phung, N.; Menzel, D.; Grischek, M.; Kegelmann, L.; Skroblin, D.; Gollwitzer, C.; Malinauskas, T.; Jost, M.; Matic, G.; Rech, B.; Schlatmann, R.; Topic, M.; Korte, L.; Abate, A.; Stannowski, B.; Neher, D.; Stolterfoht, M.; Unold, T.; Getautis, V.; Albrecht, S. Monolithic Perovskite/silicon Tandem Solar Cell with 29% Efficiency by Enhanced Hole Extraction. *Science* **2020**, *370* (6522), 1300.
(52) Liu, Y. L.; Shen, S. Y.; Prezhdo, O. V.; Long, R.; Fang, W. H. Nuclear Quantum Effects Accelerate Hot Carrier Relaxation but Slow Down Recombination in Metal Halide Perovskites. *J. Am. Chem. Soc.* **2025**, *147* (13), 11543−11554.
(53) Zhang, L. L.; Wang, Q. Y.; Wang, L. Y.; Wang, L. Y.; Zhao, J.; Li, S. F. Ultrafast Charge Transfer in Anisotropic Black Phosphorus/TiS_3 Heterostructures for Photoconversion. *Phys. Rev. B* **2024**, *109* (7), 9.
(54) Pei, W.; Wang, Z.; Xia, W. Z.; Huang, Z. J.; Wang, P. J.; Liu, Y. F.; Zhou, S.; Tu, Y. S.; Zhao, J. J. Rational Design of Full-Color Fluorescent C_3N Quantum Dots. *J. Phys. Chem. Lett.* **2024**, *15* (4), 1161−1171.
(55) Li, W.; Tang, J. F.; Casanova, D.; Prezhdo, O. V. Time-Domain ab lnitio Analysis Rationalizes the Unusual Temperature Dependence of Charge Carrier Relaxation in Lead Halide Perovskite. *ACS Energy Lett.* **2018**, *3* (11), 2713−2720.
(56) Craig, C. F.; Duncan, W. R.; Prezhdo, O. V. Trajectory Surface Hopping in The Time-dependent Kohn-Sham Approach for Electron-nuclear Dynamics. *Phys. Rev. Lett.* **2005**, *95* (16), 4.
(57) Zheng, Q. J.; Chu, W. B.; Zhao, C. Y.; Zhang, L. L.; Guo, H. L.; Wang, Y. N.; Jiang, X.; Zhao, J. Ab Initio Nonadiabatic Molecular Dynamics Investigations on The Excited Carriers in Condensed Matter Systems. *Wiley Interdiscip. Rev.-Comput. Mol. Sci.* **2019**, *9* (6), 27.
(58) Prezhdo, O. V.; Rossky, P. J. Relationship Between Quantum Decoherence Times and Solvation Dynamics in Condensed Phase Chemical Systems. *Phys. Rev. Lett.* **1998**, *81* (24), 5294−5297.
(59) Xu, X. H.; Han, X.; Stippell, E.; Fang, W. H.; Prezhdo, O. V.; Long, R. Anisotropic Exciton-Polariton Relaxation and Phonon Bottleneck in Microcavity-Confined Metal Halide Perovskites: Ab Initio Quantum Dynamics. *Nano Lett.* **2025**, *25* (34), 13063−13069.
(60) Ma, X. B.; Liu, Z. H.; Fang, W. H.; Long, R.; Prezhdo, O. V. Passivation of Hydrogen Interstitials in Metal Halide Perovskites: A Time-Domain Ab Initio Study. *J. Am. Chem. Soc.* **2025**, *147* (29), 25960−25968.
(61) Yao, Y. S.; Li, Q. Q.; Chu, W. B.; Ding, Y. M.; Yan, L.; Gao, Y.; Neogi, A.; Govorov, A.; Zhou, L. J.; Wang, Z. M. Exploration of the origin of the excellent charge-carrier dynamics in Ruddlesden-Popper oxysulfide perovskite $Y_2Ti_2O_5S_2$. *Phys. Chem. Chem. Phys.* **2023**, *25* (48), 32875−32882.
(62) Tu, Y. Y.; Chu, W. B.; Shi, Y. L.; Zhu, W. G.; Zheng, Q. J.; Zhao, J. High Photoreactivity on a Reconstructed Anatase TiO_2 (001) Surface Predicted by Ab Initio Nonadiabatic Molecular Dynamics. *J. Phys. Chem. Lett.* **2022**, *13* (25), 5766−5775.
(63) Wu, S. Y.; Ma, J. Z.; Zhang, C. W.; Prezhdo, O. V.; Zhao, J.; Gong, X. G.; Chu, W. B. Photocatalysis at the Molecule/Metal Oxide Interface Is Driven by Asymmetric Photocarrier Transfer: Ab Initio Quantum Dynamics Simulation. *J. Am. Chem. Soc.* **2025**, *147* (24), 21060−21067.
(64) Richter, A. F.; Binder, M.; Bohn, B. J.; Grumbach, N.; Neyshtadt, S.; Urban, A. S.; Feldmann, J. Fast Electron and Slow Hole Relaxation in InP-Based Colloidal Quantum Dots. *ACS Nano* **2019**, *13* (12), 14408−14415.
(65) Kang, D. G.; Won, Y. H.; Park, C.; Han, Y.; Kim, S. K. The Effect of the Mid-Shell Thickness on the Charge-Carrier Dynamics of the Green-Light Emitting InP/ZnSe/ZnS Core-Shell Quantum Dots. *Adv. Mater. Interfaces* **2024**, *11* (2), 9.
(66) Kim, T.; Won, Y.-H.; Jang, E.; Kim, D. Negative Trion Auger Recombination in Highly Luminescent InP/ZnSe/ZnS Quantum Dots. *Nano Lett.* **2021**, *21* (5), 2111−2116.
(67) Jin, H.; Livache, C.; Kim, W. D.; Diroll, B. T.; Schaller, R. D.; Klimov, V. I. Spin-exchange carrier multiplication in manganese-doped colloidal quantum dots. *Nat. Mater.* **2023**, *22* (8), 1013.
(68) Lin, C. C.; Liu, T. R.; Lin, S. R.; Boopathi, K. M.; Chiang, C. H.; Tzeng, W. Y.; Chien, W. H. C.; Hsu, H. S.; Luo, C. W.; Tsai, H. Y.; Chen, H. A.; Kuo, P. C.; Shiue, J.; Chiou, J. W.; Pong, W. F.; Chen, C. C.; Chen, C. W. Spin-Polarized Photocatalytic CO_2 Reduction of Mn-Doped Perovskite Nanoplates. *J. Am. Chem. Soc.* **2022**, *144* (34), 15718−15726.
(69) Kim, T. W.; Choi, K.-S. Nanoporous $BiVO_4$ Photoanodes with Dual-Layer Oxygen Evolution Catalysts for Solar Water Splitting. *Science* **2014**, *343* (6174), 990−994.
(70) Zhang, Y. J.; Xu, L. C.; Liu, B. Y.; Wang, X.; Wang, T. S.; Xiao, X.; Wang, S. C.; Huang, W. Engineering $BiVO_4$ and Oxygen Evolution Cocatalyst Interfaces with Rapid Hole Extraction for Photoelectrochemical Water Splitting. *ACS Catal.* **2023**, *13* (9), 5938−5948.

https://doi.org/10.1021/acsenergylett.6c00616
ACS Energy Lett. 2026, 11, 4465−4474